coatings

MDPI

*Article*

# Determining the Annealing Temperature Dependency of Wetting and Mechanical Features on $Fe_3Si$ Films

**Nattakorn Borwornpornmetee [1], Chawapon Achirawongwat [1], Thawichai Traiprom [2], Bunpot Saekow [3], Supanit Porntheeraphat [3], Boonchoat Paosawatyanyong [4], Tsuyoshi Yoshitake [5] and Nathaporn Promros [1,*]**

[1] Department of Physics, School of Science, King Mongkut's Institute of Technology Ladkrabang, Bangkok 10520, Thailand; 65056032@kmitl.ac.th (N.B.); 62050682@kmitl.ac.th (C.A.)
[2] Program of Science for industry, Faculty of Science, Chulalongkorn University, Bangkok 10330, Thailand; 6572035023@student.chula.ac.th
[3] Digital Agriculture Technology Research Team, National Electronics and Computer Technology Center, Pathumthani 12120, Thailand; bunpot.saekow@nectec.or.th (B.S.); supanit.porntheeraphat@nectec.or.th (S.P.)
[4] Department of Physics, Faculty of Science, Chulalongkorn University, Bangkok 10330, Thailand; boonchoat.p@chula.ac.th
[5] Department of Advanced Energy Science and Engineering, Kyushu University, Fukuoka 816-8580, Japan; tsuyoshi_yoshitake@kyudai.jp
* Correspondence: nathaporn_promros@kyudai.jp; Tel.: +66-80-345-3642

**Abstract:** The impact of thermal annealing under temperature alteration on the wetting and mechanical attributes of $Fe_3Si$ films built through facing target sputtering (FTS) is an essential topic for study in order to identify their characteristics under varying temperatures. Consequently, we introduced a thermal annealing process in a vacuum for two hours under varying temperatures of 300, 600, and 900 °C to our $Fe_3Si$ films created via FTS. The primary purpose of this current research is to examine the effect of the thermal annealing technique under temperature alteration on the wetting and mechanical traits of $Fe_3Si$ films. In this research, $Fe_3Si$ films were built onto the Si wafer by FTS and divided for use in thermal annealing under temperature alteration. The structural, morphological, wetting, and mechanical traits of the $Fe_3Si$ films under thermal annealing are provided in the present work. Based on our information, this work represents an original study on the change in wetting and mechanical traits of $Fe_3Si$ films through thermal annealing under temperature alteration.

**Keywords:** $Fe_3Si$ film; facing targets sputtering; wettability; mechanical property; annealing

check for updates

**Citation:** Borwornpornmetee, N.; Achirawongwat, C.; Traiprom, T.; Saekow, B.; Porntheeraphat, S.; Paosawatyanyong, B.; Yoshitake, T.; Promros, N. Determining the Annealing Temperature Dependency of Wetting and Mechanical Features on $Fe_3Si$ Films. *Coatings* **2023**, *13*, 1328. https://doi.org/10.3390/coatings13081328

Academic Editor: Fábio Ferreira

Received: 15 June 2023
Revised: 24 July 2023
Accepted: 25 July 2023
Published: 28 July 2023



## 1. Introduction

Ferromagnetic silicide ($Fe_3Si$), composed of naturally available materials (Si and Fe), is known to be appealing in the plausible application of spin transistors and self-cleaning surfaces [1–4]. Prior related studies show that the epitaxial production of $Fe_3Si$ films onto 111-oriented Si wafers can be achieved via the usage of facing target sputtering (FTS) [5,6]. The $Fe_3Si$ films own the 4.2% misfit of the lattice parameter for Si and three different bcc-like structures (D03, B2, A2) for $Fe_3Si$ to exist [5,6]. The $Fe_3Si$ films possess a striking magnetic attribute of a small coercive field (7.5 Oe) and a high spin polarization (45%) [7–9]. They also own a noticeable thermal stability above an 800 K Curie temperature [7–9]. The $Fe_3Si$ films own corrosion resistance and a high degree of hardness [10–12]. With these promising attributes, $Fe_3Si$ is a plausible candidate for ferromagnetic material, self-cleaning surfaces, and hard coatings [1]. The magnetic and structural attributes of $Fe_3Si$ films have been explored and reported in prior studies [2–4]. Nevertheless, the wettability and mechanical attributes of the $Fe_3Si$ films including the influence of an annealing temperature have barely been studied until now.

Upon a review of previous studies, the research team involved in this current work reported the epitaxial production of the $Fe_3Si$ film layer onto 111-oriented Si wafers utilizing the FTS appliance [1–4]. In principle, the FTS appliance has two equally sized circular targets facing each other, placed far from a substrate holder [13–16]. The advantages of the FTS are that it creates high plasma density, operates under low pressure, suffers little plasma damage, has a smooth surface, and exhibits little stoichiometry change [13–16]. The influence of temperature heated at the substrate on $Fe_3Si$ film growth was formerly studied [3]. At a substrate temperature of 300 °C, the crystallinity of $Fe_3Si$ films increased and retained its phase [3]. Xie et al. [17] reported dependency on the annealing temperature of $Fe_3Si$ film's properties. The $Fe_3Si$ films are fabricated onto $SiO_2$ by resistive thermal evaporation and annealed at temperatures ranging from 700 to 950 °C. The films initially possessed a crystalline structure of $Fe_{0.9}Si_1$ and then developed into that of the $Fe_3Si$ phase after annealing at 850 °C or higher. In comparison, our method of FTS epitaxy could form $Fe_3Si$ at room temperature without the need for annealing. Recently, the author reported the employment of argon (Ar) plasma etching by varying the etching power to modify the surface as well as the chemical composition over the surface of $Fe_3Si$ films [1]. The hydrophobic behavior of the untreated $Fe_3Si$ layer surface was found to turn into a hydrophilic surface through etching at 150 W of power [1]. Nevertheless, the surface property of $Fe_3Si$ films needs to be further studied to identify its novel characteristics.

Based on the literature review, thermal annealing plays a primary role in modifying the physical attributes of thin films, such as enhancing the crystallinity, crystallite size, and surface roughness of the films as well as wettability [18–21]. According to a previous report, Raj et al. annealed the BFO thin films under different annealing times, resulting in the increment of grain size and roughness as the temperature increased [19]. Bazhan et al. reported the influence of different annealing temperatures on the wettability of iron oxide films [20]. An increment in temperature induces the transition of the phase and surface topology of iron oxide films, increasing the contact angle of the film's surface [20]. Until now, reports on the influence of annealing as an extension of the wettability and mechanical attributes of $Fe_3Si$ films created utilizing FTS are extremely scarce.

The influence of temperature in the annealing procedure on the wettability and mechanical attributes of $Fe_3Si$ films is an essential topic for study to provide their annealing characteristics under varying temperatures. Thus, the characteristics of the $Fe_3Si$ film attributes after annealing in a vacuum for two hours at different annealing temperatures of 300 °C, 600 °C, and 900 °C are revealed in the current study. To the best of the author's information and knowledge, this current study is the first on the characteristics of wettability and mechanical attributes of $Fe_3Si$ films after annealing at different temperatures.

## 2. Materials and Methods

### 2.1. Production of $Fe_3Si$ Films

The n-type 111-oriented Si wafer (SUMCO Corporation) with a resistivity of 1000–4000 ohm·cm was used as a substrate for producing the $Fe_3Si$ film. The oils and organic residues on the Si sample were cleaned utilizing two acetone and methanol solvents obtained from the Fujifilm Wako Pure Chemical Corporation. Next, the native silicon dioxide on the Si sample surface was removed using 1% hydrofluoric acid. Deionized water was then employed to rinse the hydrofluoric acid from the Si sample surface. Finally, nitrogen gas (99.999% purity) obtained from the Iwatani Corporation was used for blow drying the Si wafer. Two equally sized circular $Fe_3Si$ alloy targets (99.9% purity) purchased from TOSHIMA Manufacturing Co., Ltd. were used in the sputtering process. A rotary pump (model: CIT-Alcatel 2030C) obtained from Alcatel Japan and a turbo molecular pump (model: TG1003) obtained from Osaka Vacuum were used to vacuumize the FTS chamber for sputtering. For the $Fe_3Si$ deposition procedure, the base pressure was achieved with a value below $3 \times 10^{-5}$ Pascal. A sputtering pressure with a value of $1.33 \times 10^{-1}$ Pascal was achieved after feeding Ar gas (99.9999% purity) obtained from the Iwatani Corporation into the inside of the FTS chamber. The Ar gas flow rate was 15 sccm. The temperature at the rear of the Si sample was fixed at 300 °C through the temperature controller (model: E5CN) purchased from OMRON. A voltage of 1 kV for the gas discharge process was fixed via a DC power source (model: HD1K-30N) purchased from Micro Denshi. A current of around 1.2 mA was generated during the sputtering process. After sputtering for 24 h, the rate of $Fe_3Si$ film production was 0.57 nm/min. The low pressure and low deposition rate during sputtering are the key that allows FTS to precisely coat $Fe_3Si$ at low temperatures as reported by our past work, where K. Sakai et. al. were able to epitaxially coat the $Fe_3Si$ on $FeSi_2$ with a deposition rate of 0.62 nm/min at an ambient temperature [4]. This precision and energy allow the epitaxy mechanism to occur without the need for external thermal energy [2].

### *2.2. Post Annealing of $Fe_3Si$ Films*

After completing the sputtering process, the $Fe_3Si$ films were separated into four pieces in the case of non-annealing and annealing at 300 °C, 600 °C, and 900 °C temperatures. In the annealing process, the $Fe_3Si$ films were positioned on the inside of the quartz tube. Through the operation of a mechanical pump (Leybold, Bonner, Germany, Trivac D2.5) and a turbomolecular pump (Leybold, TW70 H), the base pressure inside the quartz tube was vacuumized below $3 \times 10^{-6}$ mbar. The temperature and annealing period were set through the temperature controller (Shimaden, SR53, Tokyo, Japan). The period for annealing under the current study conditions was two hours.

### *2.3. Investigation of the Properties of $Fe_3Si$ Films*

An X-ray diffractometer (XRD; Model: Rigaku, TTRAX III, Tokyo, Japan) was utilized to investigate the crystallographic features of the as-produced and annealed $Fe_3Si$ films. The measurement was performed in the grazing incidence mode ($2\theta$ scan) with a fixed incidence angle of 2°. To confirm the crystallinity, the crystallite size was simulated using JADE software by a function of Scherrer's equation. A SU 8230 Field Emission Scanning Electron Microscope (FESEM, Hitachi, Tokyo, Japan) and an XE-120 Atomic Force Microscope (AFM, Park Systems, Suwon, Korea) were employed to investigate the morphology and roughness of the as-produced and annealed $Fe_3Si$ film surface. The Hitachi S-4700 Scanning Electron Microscope was utilized to study the cross-sectional view of as-produced and annealed $Fe_3Si$ films. The Contact Angle OCA 20 appliance (DataPhysics, San Jose, CA, USA) was used to measure the contact angles of the unannealed and annealed $Fe_3Si$ film surface. A nanoindenter (model: Ti premier) obtained from Bruker's Hysitron (Minneapolis, MN, USA) was employed to measure the mechanical attributes of the non-annealing and annealing $Fe_3Si$ films.

## 3. Results and Discussion

### *3.1. XRD Results of $Fe_3Si$ Films*

The measured XRD patterns of the $Fe_3Si$ films without annealing and under the annealing procedure with fixed temperatures of 300 °C, 600 °C, and 900 °C are shown in Figure 1, while the list of preferred orientation of Fe-Si based materials can be referred in Table 1. In the case of $Fe_3Si$ films without annealing, the preferred crystal orientations of $Fe_3Si$ (111), $Fe_3Si$ (220), $Fe_3Si$ (222), $Fe_3Si$ (400), and $Fe_3Si$ (422) were observed at 28.50°, 44.38°, 56.28°, 64.72°, and 82.06°, respectively [2,3,11]. The strongly preferred orientations of $Fe_3Si$ (222) in comparison to the fundamental peaks of $Fe_3Si$ (111), $Fe_3Si$ (220), $Fe_3Si$ (400), and $Fe_3Si$ (422) indicate that the film's structure was predominantly occupied by a B2 structure superlattice [2]. Among homogeneous iron silicide phases of different stoichiometry, $Fe_3Si$ is the sole well-ordered phase of the Fe-rich composition. As shown in Figure 2, $Fe_3Si$ exists in the bulk phase at room temperature and is stable from there up to the melting point [5]. Hypothetically, $Fe_3Si$ with a different order of Si atom arrangement, such as the B2 structure, can also have similar properties to D03. The B2 (= CsCl) phase, where either Fe or Si randomly occupy the C sites and B sites, will replace the D03 phase when the Si concentration is below the threshold [5,6]. In our work, we formed the $Fe_3Si$ at room temperature to prevent the inter-diffusion of Fe to Si from thermal energy, resulting in a B2 structure [2]. At an annealing temperature of 300 °C, the obtained preferential orientations were observed to be in the same positions as without annealing. However, an increase in peak intensity was detected after annealing at 300 °C. This is due to the Fe atoms gaining activation energy by annealing, allowing lower surface energy atoms to diffuse to a site in the crystal lattice with favorable energy [18]. Afterward, the crystallites grew in the preferred direction and the crystallinity of the film was improved [18]. After annealing at 600 °C, an intense peak of Si (111) was clearly observed at 28.44°. In contrast, the peak intensity of $Fe_3Si$ (111) and $Fe_3Si$ (222) disappeared. After gradually providing thermal energy by conventional annealing, the structure implied to undergo a transition into a D03 structure [6]. The peak of the semiconducting phase ($\beta$-$FeSi_2$) of $\beta$ (202)/(220) at 29.12° also appeared [22–25]. Since Fe has a significantly higher diffusion coefficient than Si, the Fe atoms could diffuse into the Si layer with the application of sufficient diffusion energy [26–28]. Therefore, an improvement in the crystallinity of the film along with the phase transition was observed during annealing at 600 °C [26–28]. Subsequently, the crystalline orientation shifted further with a higher activation energy from annealing at 900 °C. The $\beta$ (202)/(220) evolved dramatically, causing a superposition between itself and Si(111). At the same time, several peaks of $\beta$ (400), $\beta$ (331), $\beta$ (422), and $\beta$ (333) appeared at 34.72, 45.20, 49.80, and 58.90°, respectively [22,29]. When annealing further, the sample at the phase above the ideal Si concentration of the D03 structure can retain the phase from the boundary of 26% at RT to 31% at 1200 °C, even when an absurd phase transition occurs [5]. The FeSi phase will only appear when the Fe and Si atom's structure themselves in the almost 1:1 composition [5,6]. Meanwhile, the $\beta$ phase could mainly form when Si concentration is around 67% at temperatures below 950 °C. Also, the $\beta$ phase could appear with periodic stoichiometry deviations after atomic segregation and diffusion at the $Fe_3Si$ surface [5]. According to the estimation, the crystallite size of the $Fe_3Si$ films without annealing was 22.69 nm. The estimated values for the crystallite size were improved to 33.97, 34.71, and 37.98 nm under fixed annealing temperatures of 300 °C, 600 °C, and 900 °C, respectively. In contrast to the result reported by Xie et al. [17], the annealing reduces our film's $Fe_3Si$ structure rather than enhances the structure. This should be taken into account that our circumstances are wildly different since our films were B2 structured $Fe_3Si$ on Si (111) substrate. The combination of the high diffusion coefficient of Fe in Si combined with the structure defect allows our films to phase shift to compensate for those downsides [30,31]. On the other hand, Xie et al.'s sample was bcc-structured $Fe_3Si$ resulting from the 700 °C annealing of the thermally evaporated sample on the $SiO_2$ before turning into fcc-structured $Fe_3Si$ by thermal annealing of 950 °C [17]. Si has a high diffusion coefficient against the $SiO_2$, while diffusion rate of Fe against $SiO_2$ is dwarfed by that of Fe against Si [32,33]. Hence, the misaligned Fe-Si structure and stoichiometry of the evaporated films were corrected resulting in enhancement by increasing the temperature rather than a phase shifting through interdiffusion like in our case [34].

**Table 1.** The crystal orientation of non-annealed $Fe_3Si$ films along with annealed $Fe_3Si$ films at 300 °C, 600 °C, and 900 °C.

| Angle | Orientation | Reference |
|---|---|---|
| 28.50 | $Fe_3Si$ (111) | [8] |
| 29.12 | $\beta$ (202)/(220) | [19–22] |
| 34.72 | $\beta$ (400) | [19] |
| 44.38 | $Fe_3Si$ (220) | [8] |
| 45.20 | $\beta$ (331) | [19] |
| 49.80 | $\beta$ (422) | [26] |
| 56.28 | $Fe_3Si$ (222) | [2] |
| 58.90 | $\beta$ (333) | [26] |
| 64.72 | $Fe_3Si$ (400) | [8] |
| 82.06 | $Fe_3Si$ (422) | [8] |

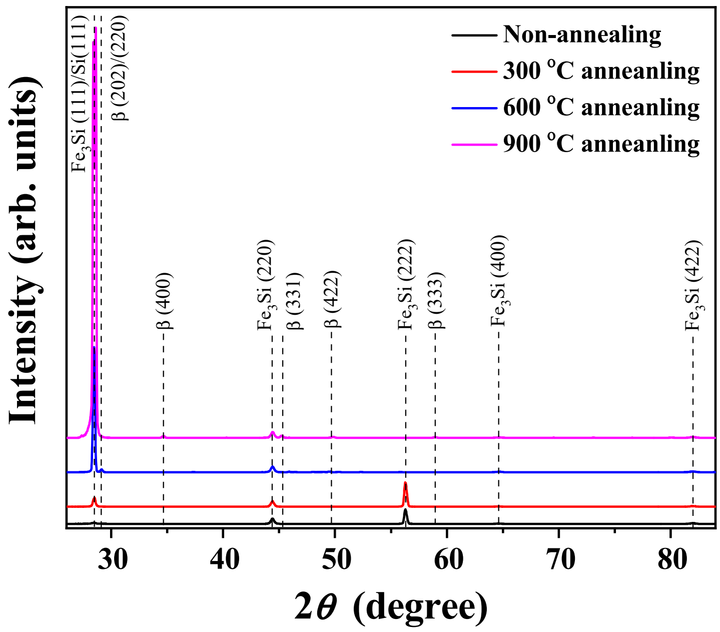


**Figure 1.** The measured XRD spectra of non-annealed $Fe_3Si$ film along with annealed $Fe_3Si$ films at 300 °C, 600 °C, and 900 °C.

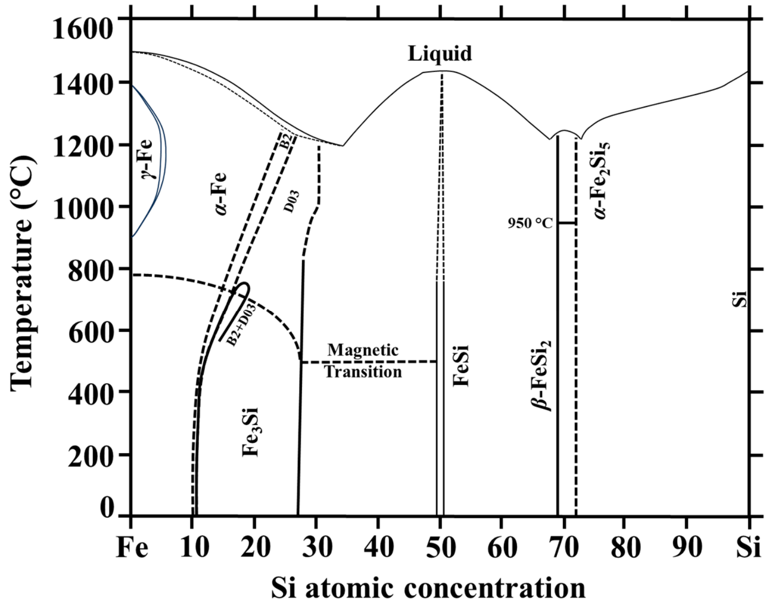


**Figure 2.** Phase diagram of Fe-Si material as a function of temperature versus Si atomic concentration.

### *3.2. FESEM Results of $Fe_3Si$ films*

The FESEM images of the surface morphology together with cross sections of $Fe_3Si$ films without annealing and annealed under various temperatures are displayed in Figure 3. From the FESEM images in plane view, the $Fe_3Si$ films without annealing and annealing at 300 °C exhibited a smooth surface consisting of many tiny uniform crystallites. The tiny crystallites with surface uniformity merged together and became nanocrystalline clusters with an annealing temperature of 600 °C. In addition, a void increment can be observed in the midst of the generated nanocrystalline clusters. At an annealing temperature of 900 °C, many tiny crystallites were completely clustered, leading to many bigger clusters. Xie et al. [17] also report a significant change of surface morphology after annealing, where their $Fe_3Si$ films possess an island-like morphology at 700 °C similar to ours at 600 °C. Then, 950 °C turns separated crystallites into clustered, like we observe at 900 °C.

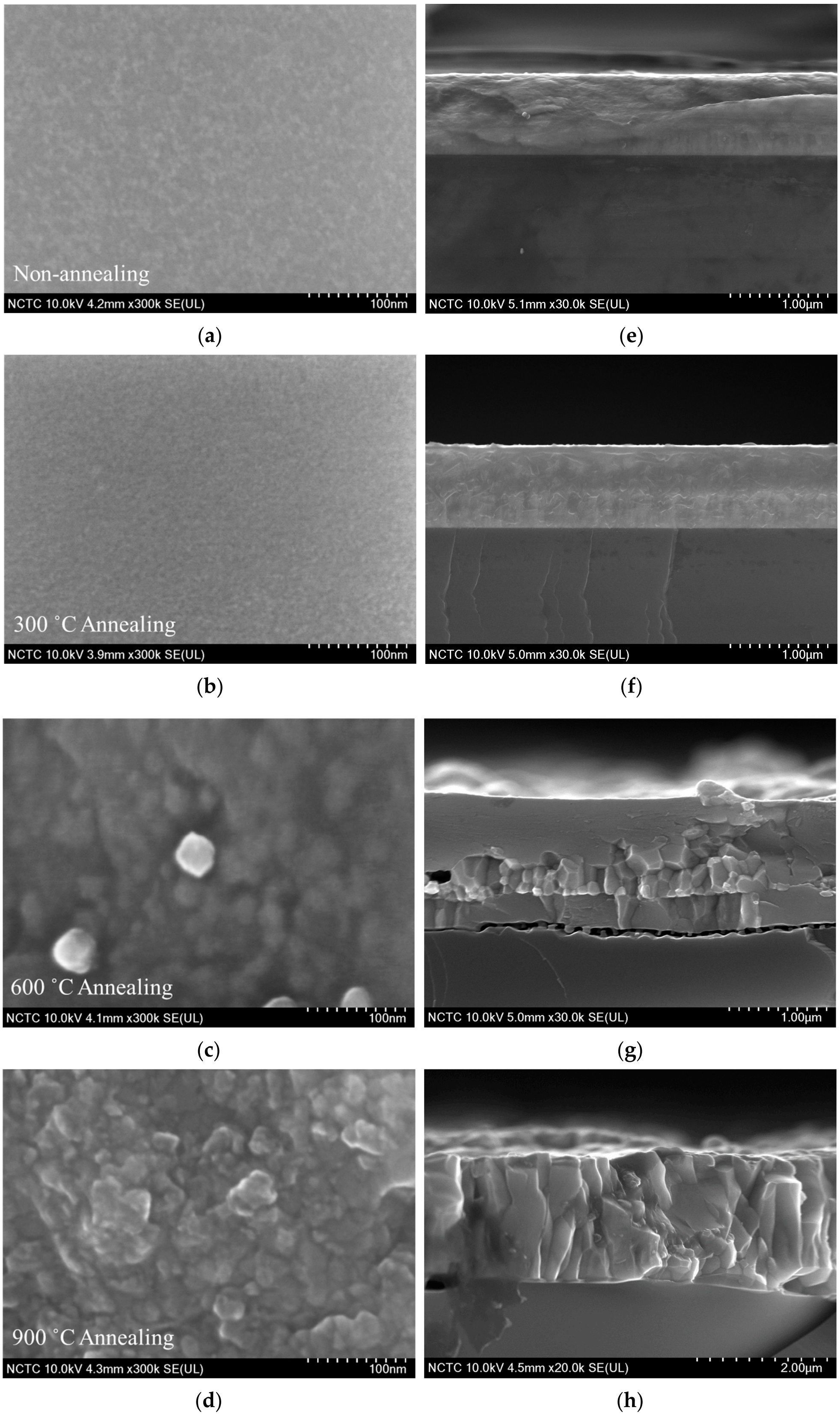


**Figure 3.** FESEM images of $Fe_3Si$ film surfaces (**a**) without annealing and annealing (**b**) 300 °C, (**c**) 600 °C, (**d**) 900 °C in plane-view. The cross-sectional images of Fe3Si films present in (**e**) for unannealed films along with (**f**) for 300 °C annealed films, (**g**) for 600 °C annealed films, and (**h**) for 900 °C annealed films.

The FESEM cross-sectional images of the $Fe_3Si$ films for non-annealing and annealing at a temperature of 300 °C showed a sharp interface between the produced films and the Si wafers. In addition, the unannealed $Fe_3Si$ films exhibited a smooth surface which changes slightly after annealing at 300 °C. After annealing at 600 °C and 900 °C, the interface became uneven. A rough surface on the $Fe_3Si$ films can be observed due to the creation of several big clustered crystalline structures together with pinholes on the $Fe_3Si$ film surface.

### 3.3. AFM Results of $Fe_3Si$ Films

AFM topographic images of the $Fe_3Si$ film surface in the case of non-annealing and annealed under temperature values set at 300 °C, 600 °C, and 900 °C are depicted in Figure 4. For non-annealing $Fe_3Si$ film, an extremely smooth surface was observed with an estimated root-mean-square (RMS) roughness of 0.588 nm as shown in Table 2. In the case of film fabrication via FTS, the plasma zone was far from the Si wafer on the substrate holder [13–16]. Thus, the plasma caused very little damage by plasma to the $Fe_3Si$ film surface [13–16]. The temperature of the film surface during film production did not increase. For these reasons, the $Fe_3Si$ film surface was quite smooth. After annealing at 300 °C, the RMS roughness increased slightly to 0.743 nm. The RMS roughness increased dramatically to 98.235 and 113.361 nm under annealing temperatures fixed at 600 °C and 900 °C, respectively. Based on the FESEM images, big clusters and pinholes were formed in the case of annealing temperatures set at 600 °C and 900 °C. Thus, the $Fe_3Si$ film surfaces after annealing under these temperatures were rougher than those under lower temperatures and non-annealing.

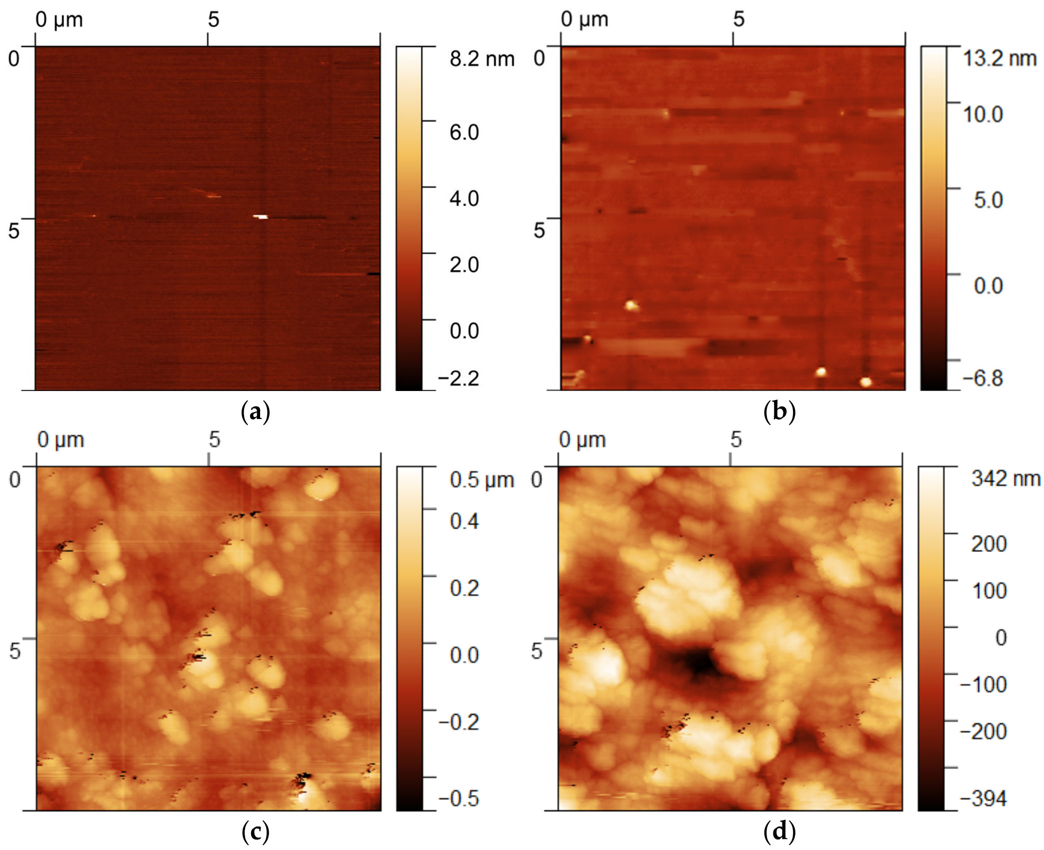


**Figure 4.** AFM topographic images of $Fe_3Si$ film surfaces (**a**) without annealing and annealing (**b**) 300 °C, (**c**) 600 °C, and (**d**) 900 °C.

**Table 2.** The values of RMS roughness of $Fe_3Si$ films without annealing and through annealing at fixed temperatures of 300 °C, 600 °C, and 900 °C.

| Annealing Temperature (°C) | RMS Roughness (nm) |
|---|---|
| Non-annealing | 0.588 |
| 300 | 0.743 |
| 600 | 98.235 |
| 900 | 113.361 |

### *3.4. Contact Angles of $Fe_3Si$ Films*

In this work, the measurement of the contact angle in the midst of the droplet and the $Fe_3Si$ film surface was carried out to determine the wetting behavior of the $Fe_3Si$ film surface under annealed and unannealed conditions. Normally, the hydrophilicity can be defined by the acquired contact angle values measured in the range of $10° < \theta < 90°$ [35–37]. For hydrophobicity, the measured contact angle values are in the range of $90° < \theta < 150°$ [35–37]. Superhydrophilic and superhydrophobic are defined as the values of the contact angle measured in the range of $\theta < 10°$ and $\theta > 150°$, respectively [35–37].

The contact angles in the midst of the droplet and surface for the as-produced and annealed $Fe_3Si$ films are displayed in Figure 5. The contact angles of the $Fe_3Si$ film surface without annealing and with annealing at 300 °C were 95.8° and 95.5°, respectively. These contact angle values show that the $Fe_3Si$ film surfaces are hydrophobic under these conditions. Several porous regions between the crystallites can be seen on the FESEM image of the unannealed and annealed $Fe_3Si$ films at 300 °C. According to the model of Cassie and Baxter, the porous region performs like an air pocket, allowing air to enter the grooves and assist in the buoyancy of the liquid [38,39]. This leads to a higher contact angle value than for a flat surface. A decrement in contact angles was found with annealing under fixed temperatures of 600 °C and 900 °C with values of 80.6° and 77.9°, respectively. This suggests the transition from the Cassie and Baxter model to the Wenzel model for the $Fe_3Si$ film surface [40,41]. The spaces in the midst of the nanostructures are filled by water since a water/solid interface is more desirable than an air/solid interface at high annealing temperatures [40,41]. Hence, the droplet bottom possesses conformal contact with the solid surface [40,41]. This can increase the interfacial force between solids and water on the surface, leading to a decrement in the contact angle value. Therefore, the contact angles of annealed films reduced with the significantly increasing roughness are shown in Figure 5e, depicting the correlation between the contact angles and roughness of annealed films. The contact angle values of non-annealing $Fe_3Si$ films and annealing at different annealing temperatures were summarized in Table 3.

**Table 3.** Contact angle values of $Fe_3Si$ films at different annealing temperatures.

| Annealing Temperature (°C) | $\theta$ CA (°) | Wetting State |
|---|---|---|
| Non-annealed | 95.8 | Hydrophobic |
| 300 | 95.5 | Hydrophobic |
| 600 | 80.6 | Hydrophilic |
| 900 | 77.9 | Hydrophilic |

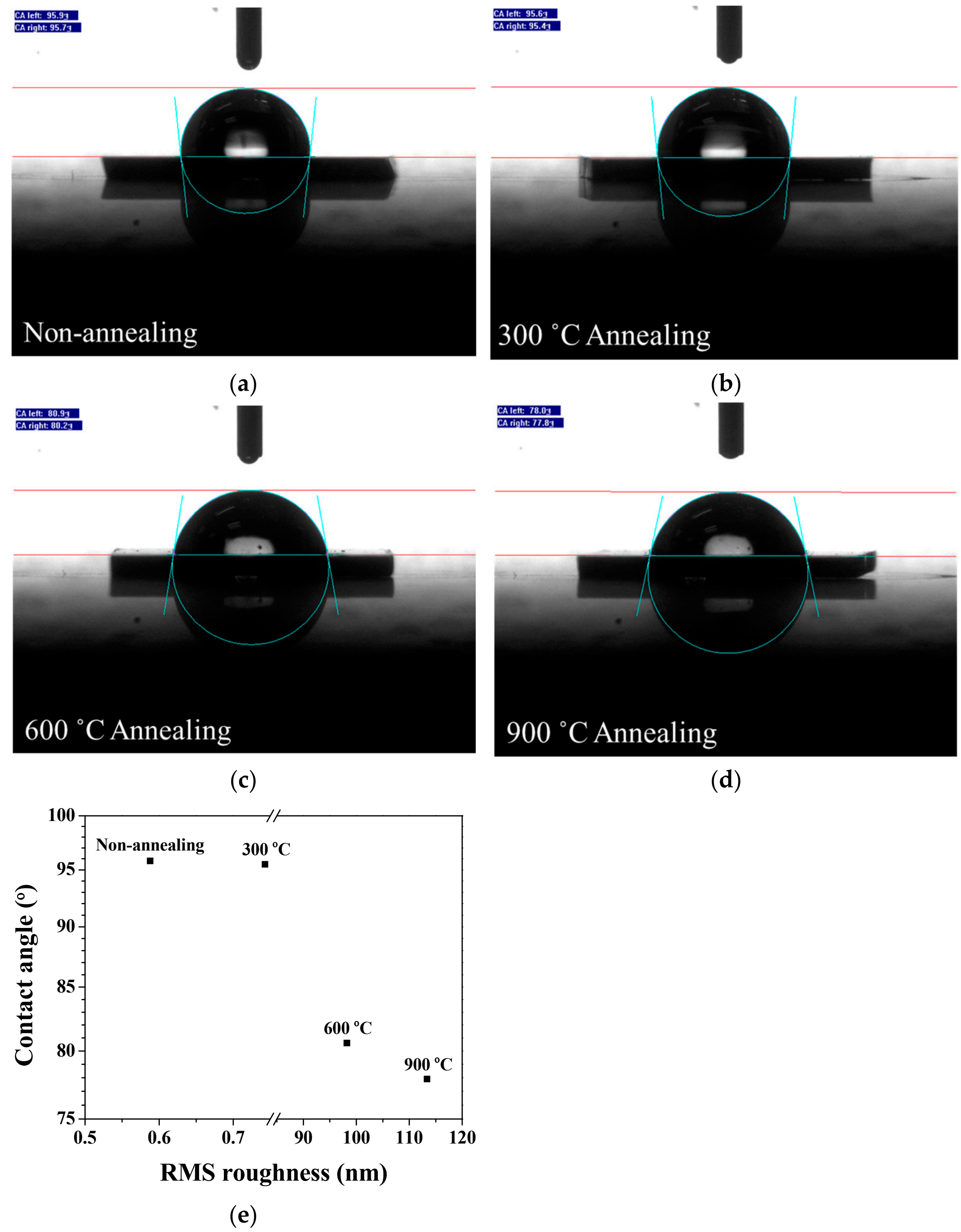


**Figure 5.** Image of the contact angle between droplet and $Fe_3Si$ film surfaces (**a**) without post-annealing and after annealing at different temperatures of (**b**) 300 °C, (**c**) 600 °C, and (**d**) 900 °C, while (**e**) shows the relation between contact angle and rms roughness.

### *3.5. Nanoindentation Results of $Fe_3Si$ Films*

A nanoindentation appliance was used with a Berkovich indenter to assess the average hardness (H) and reduced elastic modulus ($E_r$) values for the surfaces of annealed and unannealed $Fe_3Si$ films. The applied indentation load was 3 mN and the fixed maximum depth was 10% of the $Fe_3Si$ films' thickness. Figure 6 demonstrates the applied indentation load versus the depth plot for the $Fe_3Si$ films without annealing and through annealing under temperature values of 300 °C, 600 °C, and 900 °C. The values of H and $E_r$ of the annealed and unannealed $Fe_3Si$ layer surfaces were extracted from the unloading portions of their curve of load–depth [42,43]. The acquired H and $E_r$ values for the experimental conditions in this study are displayed in Table 4. The H value of unannealed $Fe_3Si$ film was 8.741 GPa. The $Fe_3Si$ films exhibited an increment in hardness values of 9.363, 14.543, and 15.341 GPa under fixed annealing temperatures of 300 °C, 600 °C, and 900 °C, respectively. An increase in the annealing temperature can enhance the grain size of the $Fe_3Si$ films. This developed grain may affect the nanoindentation mechanism by dislocation through grain boundary sliding [44–46]. Hence, the hardness result trending in the same manner as the inverse Hall–Petch effect relies heavily on the grain boundary structure of the testing material [44–46]. This sudden change in the film's morphology may also be linked to inconsistency in the hardness [47]. The $E_r$ value of $Fe_3Si$ films without annealing was approximately 184.899 GPa. The $E_r$ value exhibited the same rising trend as the hardness. In other words, the value of $E_r$ increased along with the annealing temperature. The $E_r$ values of 204.803, 271.261, and 323.187 GPa were obtained for $Fe_3Si$ films annealed at 300 °C, 600 °C, and 900 °C, respectively. The $E_r$ tends to follow the crystal orientation of the crystalline materials, aligning with the XRD results in this study [44].

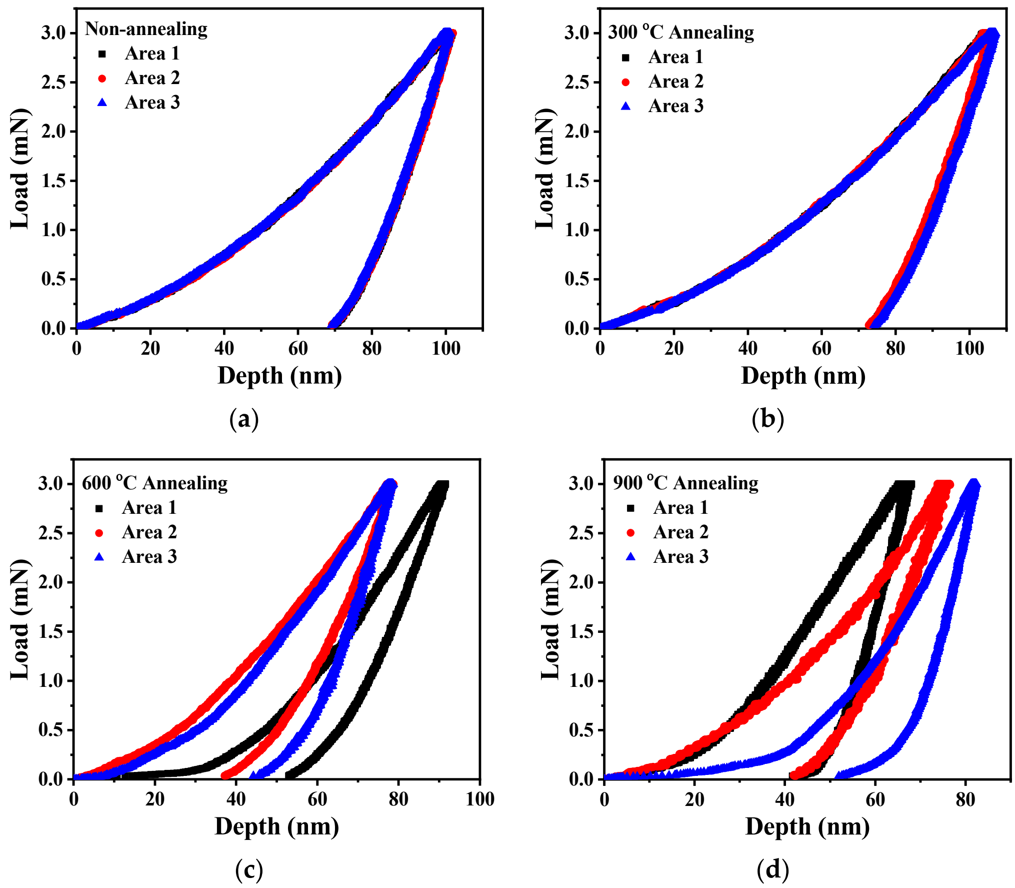


**Figure 6.** Comparison between depth and load on non-annealed and annealed $Fe_3Si$ films. (**a**) is non-annealed $Fe_3Si$ films; (**b**) is 300 °C annealed $Fe_3Si$ films; (**c**) is 600 °C annealed $Fe_3Si$ films; (**d**) is 900 °C annealed $Fe_3Si$ films.

**Table 4.** H and $E_r$ values of $Fe_3Si$ films at different annealing temperatures.

| Annealing Temperature (°C) | H (GPa) | $E_r$ (GPa) |
|---|---|---|
| Without annealing | 8.741 ± 0.111 | 184.899 ± 1.343 |
| 300 | 9.363 ± 0.081 | 204.803 ± 1.347 |
| 600 | 14.543 ± 0.983 | 271.261 ± 34.495 |
| 900 | 15.341 ± 1.777 | 323.187 ± 89.125 |

## 4. Conclusions

This study reveals the results of the thermal annealing process under fixed temperatures of 300 °C, 600 °C, and 900 °C for the modification of wettability, surface morphology, and mechanical attributes of $Fe_3Si$ films produced through FTS. According to the XRD measurement, several preferred crystal orientations can be observed for $Fe_3Si$ films without annealing and those annealed at 300 °C. Higher crystallinity and several preferred crystal orientations appeared in the 600 °C and 900 °C annealed $Fe_3Si$ films. According to the FESEM results, the $Fe_3Si$ films without annealing and those annealed under a fixed temperature of 300 °C exhibited a significant number of little uniform nanocrystallites. At an annealing temperature of 600 °C, they merged into little nanocrystalline clusters, huddling to generate large clusters at 900 °C. The acquired AFM images indicate that $Fe_3Si$ films without annealing and with an annealing temperature of 300 °C own a very smooth surface, having a small rms roughness which increased dramatically by annealing at temperatures above 300 °C. The average contact angle for the surface of the $Fe_3Si$ films without annealing and with annealing exhibited hydrophobic properties. It became hydrophilic after annealing at temperatures above 300 °C. The film hardness of the as-formed $Fe_3Si$ was significantly enhanced after annealing above 300 °C. It can therefore be concluded that an annealing temperature above 300 °C significantly alters the structural, morphological, wettability, and mechanical attributes of $Fe_3Si$ films.

**Author Contributions:** Conceptualization, N.P.; methodology, N.B., B.S., S.P. and N.P.; formal analysis, N.B., T.T. and N.P.; investigation, N.B., C.A., T.T. and N.P.; writing—original draft preparation, N.B., T.T. and N.P.; writing—review and editing, N.B., T.T., B.S., S.P., B.P., T.Y. and N.P.; Visualization, N.B., C.A., T.T. and N.P.; Supervision, B.P. and T.Y. All authors have read and agreed to the published version of the manuscript.

**Funding:** This work is supported by King Mongkut's Institute of Technology Ladkrabang (grant numbers KDS2022-06). The allowance for carrying out this research was provided by the Academic Research Fund, School of Science, King Mongkut's Institute of Technology Ladkrabang, with grant numbers 2562-01-05-29, 2562-01-05-44, and 2563-02-05-36.

**Institutional Review Board Statement:** Not applicable.

**Informed Consent Statement:** Not applicable.

**Data Availability Statement:** The data presented in this study are available in this article.

**Acknowledgments:** This work is supported by King Mongkut's Institute of Technology Ladkrabang. The authors also express their gratitude for the contribution and cooperation received from Research Unit of Integrated Science for Electronic, Material and Industry (ISEMI), School of Science, King Mongkut's Institute of Technology Ladkrabang.

**Conflicts of Interest:** The authors declare no conflict of interest.

## References


1. Borwornpornmetee, N.; Charoenyuenyao, P.; Chaleawpong, R.; Paosawatyanyong, B.; Phatthanakun, R.; Sittimart, P.; Aramaki, K.; Hamasaki, T.; Yoshitake, T.; Promros, N. Physical Properties of $Fe_3Si$ Films Coated through Facing Targets Sputtering after Microwave Plasma Treatment. *Coatings* **2021**, *11*, 923. [CrossRef]
2. Yoshitake, T.; Nakagauchi, D.; Ogawa, T.; Itakura, M.; Kuwano, N.; Tomokiyo, Y.; Kajiwara, T.; Nagayama, K. Room-Temperature Epitaxial Growth of Ferromagnetic $Fe_3Si$ Films on Si(111) by Facing Target Direct-Current Sputtering. *Appl. Phys. Lett.* **2005**, *86*, 262505. [CrossRef]
3. Nakagauchi, D.; Yoshitake, T.; Nagayama, K. Fabrication of Ferromagnetic $Fe_3Si$ Thin Films by Pulsed Laser Deposition Using an $Fe_3Si$ Target. *Vacuum* **2004**, *74*, 653–657. [CrossRef]
4. Sakai, K.; Noda, Y.; Tsumagari, D.; Deguchi, H.; Takeda, K.; Yoshitake, T. Temperature-Dependent Interlayer Coupling in $Fe_3Si/FeSi_2$ Artificial Lattices. *Phys. Status Solidi (A) Appl. Mater. Sci.* **2014**, *211*, 323–328. [CrossRef]
5. Starke, U.; Schardt, J.; Weiss, W.; Meier, W.; Polop, C.; de Andres, P.L.; Heinz, K. Structural and Compositional Reversible Phase Transitions on Low-Index $Fe_3Si$ Surfaces. *Europhys. Lett.* **2001**, *56*, 822. [CrossRef]
6. Gude, A.; Mehrer, H. Diffusion in the $D0_3$-Type Intermetallic Phase $Fe_3Si$. *Philos. Mag. A* **1997**, *76*, 1–29. [CrossRef]
7. Sadoh, T.; Takeuchi, H.; Ueda, K.; Kenjo, A.; Miyao, M. Epitaxial Growth of Ferromagnetic Silicide $Fe_3Si$ on Si(111) Substrate. *Jpn. J. Appl. Phys.* **2006**, *45*, 3598. [CrossRef]

8. Hamaya, K.; Ueda, K.; Kishi, Y.; Ando, Y.; Sadoh, T.; Miyao, M. Epitaxial Ferromagnetic $Fe_3Si$/Si(111) Structures with High-Quality Heterointerfaces. *Appl. Phys. Lett.* **2008**, *93*, 132117. [CrossRef]
9. Herfort, J.; Schönherr, H.-P.; Ploog, K.H. Epitaxial Growth of $Fe_3Si$/GaAs(001) Hybrid Structures. *Appl. Phys. Lett.* **2003**, *83*, 3912–3914. [CrossRef]
10. Tang, C.; Wen, F.; Chen, H.; Liu, J.; Tao, G.; Xu, N.; Xue, J. Corrosion Characteristics of $Fe_3Si$ Intermetallic Coatings Prepared by Molten Salt Infiltration in Sulfuric Acid Solution. *J. Alloys Compd.* **2019**, *778*, 972–981. [CrossRef]
11. Chang-bin, T.; Hong-xia, C.; Fu-rong, W.; Ni-jun, X.; Wei, H.; Juan-qin, X. Facile Preparation and Tribological Property of Alloyed $Fe_3Si$ Coatings on Stainless Steels Surface by Molten-Salt Infiltration Method. *Surf. Coat. Technol.* **2020**, *397*, 126049. [CrossRef]
12. Schneeweiss, O.; Pizúrová, N.; Jirásková, Y.; Žák, T.; Cornut, B. $Fe_3Si$ surface coating on SiFe steel. *J. Magn. Magn. Mater.* **2000**, *215*, 115–117. [CrossRef]
13. Lee, M.; Park, Y.; Kim, K.; Hong, J. Influence of Sputtering Conditions on the Properties of Aluminum-Doped Zinc Oxide Thin Film Fabricated Using a Facing Target Sputtering System. *Thin Solid Film.* **2020**, *703*, 137980. [CrossRef]
14. Tominaga, K.; Ueda, T.; Ao, T.; Kataoka, M.; Mori, I. ITO Films Prepared by Facing Target Sputtering System. *Thin Solid Films* **1996**, *281–282*, 194–197. [CrossRef]
15. Hossain, M.F.; Biswas, S.; Takahashi, T.; Kubota, Y.; Fujishima, A. Influence of Direct Current Power on the Photocatalytic Activity of Facing Target Sputtered $TiO_2$ Thin Films. *Thin Solid Film.* **2008**, *517*, 1091–1095. [CrossRef]
16. Jeong, J.A.; Shin, H.S.; Choi, K.H.; Kim, H.K. Flexible Al-Doped ZnO Films Grown on PET Substrates Using Linear Facing Target Sputtering for Flexible OLEDs. *J. Phys. D Appl. Phys.* **2010**, *43*, 465403. [CrossRef]
17. Xie, J.; Xie, Q.; Ma, R.; Huang, J.; Zhang, C.; Liu, D. Annealing Temperature Dependent Structures and Properties of Ferromagnetic $Fe_3Si$ Films Fabricated by Resistive Thermal Evaporation. *J. Mater. Sci. Mater. Electron.* **2018**, *29*, 1369–1376. [CrossRef]
18. Ng, Z.-N.; Chan, K.-Y.; Tohsophon, T. Effects of Annealing Temperature on ZnO and AZO Films Prepared by Sol–Gel Technique. *Appl. Surf. Sci.* **2012**, *258*, 9604–9609. [CrossRef]
19. Raj, C.A.; Muneeswaran, M.; Jegatheesan, P.; Giridharan, N.V.; Sivakumar, V.J.; Senguttuvan, G. Effect of Annealing Time in the Low-Temperature Growth of BFO Thin Films Spin Coated on Glass Substrates. *J. Mater. Sci. Mater. Electron.* **2013**, *24*, 4148–4154. [CrossRef]
20. Bazhan, Z.; Ghodsi, F.E.; Mazloom, J. Effect of Phase Transition Induced by Annealing Temperature on Wettability, Optical and Photocatalytic Properties of Nanostructured Iron Oxide Thin Film. *J. Mater. Sci. Mater. Electron.* **2018**, *29*, 11489–11497. [CrossRef]
21. Gojda, F.; Loulakis, M.; Papoutsakis, L.; Tzortzakis, S.; Chrissopoulou, K.; Anastasiadis, S.H. Altering the Surface Properties of Metal Alloys Utilizing Facile and Ecological Methods. *Langmuir* **2022**, *38*, 4826–4838. [CrossRef]
22. Terai, Y.; Yoneda, K.; Noda, K.; Miura, N.; Fujiwara, Y. Effect of Residual Impurities on Transport Properties of $\beta$-$FeSi_2$ Epitaxial Films Grown by Molecular Beam Epitaxy. *J. Appl. Phys.* **2012**, *112*, 13702. [CrossRef]
23. Tode, M.; Takigawa, Y.; Ohmukai, M.; Kurosawa, K.; Muroya, M. Epitaxially Growth of $\beta$-$FeSi_2$ Thin Films on Si(100) Substrates from $\varepsilon$-FeSi Targets with ArF Excimer Laser Deposition. *J. Phys. Conf. Ser.* **2007**, *59*, 376–379. [CrossRef]
24. Shimura, K.; Katsumata, T.; Yamaguchi, K.; Yamamoto, H.; Hojou, K. The Role of Sputter Etching and Annealing Processes on the Formation of $\beta$-$FeSi_2$ Thin Films. *Thin Solid Films* **2004**, *461*, 22–27. [CrossRef]
25. Nishikawa, Y.; Hiehata, K.; Nakamura, K. Reduction of Surface Cracks in $\beta$-$FeSi_2$ Films by Substrate Heating during RF-Sputtering Deposition. *Trans. Mat. Res. Soc. Jpn.* **2013**, *38*, 243–247. [CrossRef]
26. Lakshantha, W.J.; Dhoubhadel, M.S.; Reinert, T.; McDaniel, F.D.; Rout, B. Investigation of Various Phases of Fe–Si Structures Formed in Si by Low Energy Fe Ion Implantation. *Nucl. Instrum. Methods Phys. Res. B* **2015**, *365*, 114–119. [CrossRef]
27. Baldwin, N.R.; Ivey, D.G. Iron Slicide Formation in Bulk Iron-Silicon Diffusion Couples. *J. Phase Equilibria* **1995**, *16*, 300–307. [CrossRef]
28. Li, M.; Chen, X.; Guan, J.; Wang, J.; Liang, C. Thermally Induced Phase Transition and Magnetic Properties of Fe–$FeSi_2$ with Core–Shell Structure. *Phys. Status Solidi (A)* **2013**, *210*, 2710–2715. [CrossRef]
29. Tian, Y.; Bento Montes, A.R.; Vančo, L'.; Čaplovičová, M.; Vogrinčič, P.; Šutta, P.; Satrapinskyy, L.; Zeman, M.; Isabella, O. Toward $BaSi_2$/Si Heterojunction Thin-Film Solar Cells: Insights into Heterointerface Investigation, Barium Depletion, and Silicide-Mediated Silicon Crystallization. *Adv. Mater. Interfaces* **2020**, *7*, 2000887. [CrossRef]
30. Isobe, T.; Nakashima, H.; Hashimoto, K. Diffusion Coefficient of Interstitial Iron in Silicon. *Jpn. J. Appl. Phys.* **1989**, *28*, 1282. [CrossRef]
31. Mehrer, H. Diffusion in Intermetallics. *Mater. Trans. JIM* **1996**, *37*, 1259–1280. [CrossRef]
32. Béjina, F.; Jaoul, O. Silicon Self-Diffusion in Quartz and Diopside Measured by Nuclear Micro-Analysis Methods. *Phys. Earth Planet. Inter.* **1996**, *97*, 145–162. [CrossRef]
33. Ramappa, D.A.; Henley, W.B. Diffusion of Iron in Silicon Dioxide. *J. Electrochem. Soc.* **1999**, *146*, 3773. [CrossRef]
34. Inaba, T.; Saito, Y.; Kominami, H.; Nakanishi, Y.; Murakami, K.; Matsuyama, T.; Tatsuoka, H. Growth of $SiO_x$ Nanofibers Using FeSi Substrates with Ga Droplets. *Jpn. J. Appl. Phys.* **2006**, *45*, L1320. [CrossRef]
35. Drelich, J.; Chibowski, E.; Meng, D.D.; Terpilowski, K. Hydrophilic and Superhydrophilic Surfaces and Materials. *Soft Matter* **2011**, *7*, 9804–9828. [CrossRef]
36. Krasowska, M.; Zawala, J.; Malysa, K. Air at Hydrophobic Surfaces and Kinetics of Three Phase Contact Formation. *Adv. Colloid Interface Sci.* **2009**, *147–148*, 155–169. [CrossRef]

37. Mohamed, A.M.A.; Abdullah, A.M.; Younan, N.A. Corrosion Behavior of Superhydrophobic Surfaces: A Review. *Arab. J. Chem.* **2015**, *8*, 749–765. [CrossRef]
38. Cassie, A.B.D.; Baxter, S. Wettability of Porous Surfaces. *Trans. Faraday Soc.* **1944**, *40*, 546–551. [CrossRef]
39. Lafuma, A.; Quéré, D. Superhydrophobic States. *Nat. Mater.* **2003**, *2*, 457–460. [CrossRef] [PubMed]
40. Wenzel, R.N. Surface Roughness and Contact Angle. *J. Phys. Colloid Chem.* **1949**, *53*, 1466–1467. [CrossRef]
41. Quéré, D. Wetting and Roughness. *Annu. Rev. Mater. Res* **2008**, *38*, 71–99. [CrossRef]
42. Beegan, D.; Chowdhury, S.; Laugier, M.T. Comparison between Nanoindentation and Scratch Test Hardness (Scratch Hardness) Values of Copper Thin Films on Oxidised Silicon Substrates. *Surf. Coat. Technol.* **2007**, *201*, 5804–5808. [CrossRef]
43. Fischer-Cripps, A.C. A Review of Analysis Methods for Sub-Micron Indentation Testing. *Vacuum* **2000**, *58*, 569–585. [CrossRef]
44. Torrents, A.; Yang, H.; Mohamed, F.A. Effect of Annealing on Hardness and the Modulus of Elasticity in Bulk Nanocrystalline Nickel. *Metall. Mater. Trans. A* **2010**, *41*, 621–630. [CrossRef]
45. Swygenhoven, H. Van Grain Boundaries and Dislocations. *Science (1979)* **2002**, *296*, 66–67. [CrossRef]
46. Chen, J.; Wang, W.; Qian, L.H.; Lu, K. Critical Shear Stress for Onset of Plasticity in a Nanocrystalline Cu Determined by Using Nanoindentation. *Scr. Mater.* **2003**, *49*, 645–650. [CrossRef]
47. Chen, L.; Ahadi, A.; Zhou, J.; Ståhl, J.-E. Modeling Effect of Surface Roughness on Nanoindentation Tests. *Procedia CIRP* **2013**, *8*, 334–339. [CrossRef]